

Groundwater

Chemistry of the Karst Sarabkalan Spring, Iran, and Controls of PDO and ENSO Climate Indices on It

by Abolfazl Rezaei^{1,2}

Abstract

The Sarabkalan Spring serves as a primary water supply to irrigation and domestic use in the Sirvan Region, Iran. As it has a highly variable discharge, understanding its teleconnections with large-scale climate variability is crucial. In this study, we first characterize the springshed and its corresponding karst aquifer system using genetic algorithm analysis on the spring discharge, water balance calculations, temporal variations of physicochemical parameters, and stable isotopes along with considering its geological settings. Then, the large-scale climate indices teleconnections with precipitation and spring discharge are studied using wavelet analysis. Results reveal that the springshed contains two karst subaquifers resulting from geological and morphological settings. Unlike most developed karst systems in Zagros, which show one peak, the spring has two principal flow peaks over most hydrological years where the second peak occurs over the dry season. It takes ~99 d (from lag correlation over 2008–2019) and ~145 d (from $\delta^{18}\text{O}$ measurements over 2018–2019) for rain water to reach the Sarabkalan Spring. Moreover, intense precipitations would result in an increase in discharge and a decrease in electrical conductivity, $\text{Ca} + \text{Mg}$, HCO_3^- , SO_4^{2-} , Cl^- , ionic strength, and $\delta^{18}\text{O}$ of the spring because of the developed karst conduit(s). It is further found that a positive Pacific Decadal Oscillation phase coupled with El Niño causes an increase in both the precipitation and spring discharge, signifying the influence of the atmospheric circulations of the Pacific Ocean on the spring behavior.

Introduction

Karst terrains supply large quantities of fresh water to the world's population, currently estimated to be some 25% (Ford and Williams 2007). Commonly, the monitoring of flowrate, physicochemical parameters, and isotopic ratio compositions of spring water are used to characterize karst aquifers as they can provide valuable information about the complicated flow system of karst aquifers (Lakey and Krothe 1996; Rusjan et al. 2019). Accordingly, the literature provided in many studies characterizes karst aquifers by monitoring the water flowrates and physicochemical parameters of the springs

(Lakey and Krothe 1996; Rezaei et al. 2013; Toran and Reisch 2013; Rusjan et al. 2019).

Moreover, large-scale climate indices have a strong influence on the regional climate and hydrological variability worldwide (Huo et al. 2016). Although the effects of large-scale climate patterns on the climate variables have been studied worldwide (Huo et al. 2016; Rezaei and Gurdak 2020), their impacts on groundwater systems remain unclear in many parts of the world (Green et al. 2011).

The Sarabkalan Spring (with a high discharge of ~3.7 m³/s), the second-largest spring in Ilam Province, southwest Iran, is a primary water supply for irrigation and domestic uses. The spring has a highly variable discharge in both the long-term and seasonal scales, which can severely affect the local life. The main aims of this study are (1) to delineate the springshed, karst development, and flow system of the Sarabkalan Spring, (2) to investigate the precipitation variability control on spring flowrate, and finally (3) to explore the impact of the large-scale climate variability on the karst spring.

¹Corresponding author: Department of Earth Sciences, Institute for Advanced Studies in Basic Sciences (IASBS), 444 Prof. Yousef Sobouti Blvd., Zanjan 45137–66731, Iran; arezaei@iasbs.ac.ir; abolfazlrezaei64@gmail.com

²Center for Research in Climate Change and Global Warming (CRCC), Institute for Advanced Studies in Basic Sciences (IASBS), 444 Prof. Yousef Sobouti Blvd., Zanjan 45137–66731, Iran

Article impact statement: Beyond the local geological, morphological, and karstic factors, the karst spring behavior may be controlled by large-scale climate indices.

Received May 2020, accepted July 2020.
 © 2020, National Ground Water Association.
 doi: 10.1111/gwat.13034

Study Area

Located in Shirvan (Sirvan) Region, ~30 km east of Ilam City (Figure 1), the Sarabkalan Spring emerges

with an instantaneous mean discharge of \sim 845 L/s, varying from 135 L/s in summer 2012 up to 3668 L/s in winter 2019. Such high variability in the flowrate may predominantly result from the rainfall variability and the transformation characteristics of the system (Diodato et al. 2014). In addition to the Sarabkalan Spring, two perennial karst springs (Sero in Figure S1 in the Supporting Information [SI] and Negel in Figure 1) are drained from the Some-Khar Anticline (SKA), flowing only over high-precipitation months of wet years. The Negel Spring, with a high discharge of \sim 30 L/s, emerges from the northern limb of SKA. The Sero Spring is adjacent to the Sarabkalan Spring. Two adjacent production wells with 100 and 200 m depths had been drilled in the immediate upstream vicinity of the spring. They most probably capture some portion of the water contributing to the Sarabkalan Spring. For the water budget calculations, the average flowrate of \sim 55 L/s for the wells was also summed up by the average discharge at the spring (\sim 845 L/s).

The main geologic formations of the area, in decreasing order of age, include Pabdeh (shale and marl), Asmari (limestone), and Gachsaran (marl, gypsum, and halite). The low-permeability Pabdeh Formation, overlain by the karstic Asmari Formation (Figure 1a), constitutes the core of the Seivan Anticline (SA), SKA, and Charmin Anticline and acts as a barrier to groundwater flow in the Zagros Mountains (Rezaei et al. 2017). The evaporative-rich Gachsaran Formation broadly covers the hillsides of anticlines. The Sarabkalan Spring emerges from the SKA's plunge and classified as "down-plunge nose" according to Ashjari and Raeisi's classification (2006) (Figure 1b and Figure S2 in SI).

Methodology

This study is carried out in two phases, the details of which are explained in the "Methodology in further details" section in SI. Briefly put, the first phase of the study examines the characteristics of the karst hydrogeological system using the discharge (from 2008 to 2019), physicochemical parameters, and stable isotopes ($\delta^2\text{H}$ and $\delta^{18}\text{O}$) of the spring's water in combination with considering geological settings. A total of 102 hydrochemistry (from October 2015 to September 2019) and 29 isotope water samples were collected and analyzed for the Sarabkalan Spring. A total of 18 isotope samples were also taken from the rainfall in 2018–2019 which was the highest annual precipitation over the most four recent decades (Figure S3). For the comparison, one hydrochemistry and one isotopic water sample were collected from the Negel Spring on April 2, 2019. Moreover, two hydrochemistry (April 2 and May 10, 2019) and three isotope (February 2, April 2, and May 10, 2019) water samples were taken from the Sero Spring.

In the second phase, thanks to the applied continuous wavelet transform (CWT) and the wavelet coherence (WTC), the El Niño Southern Oscillation (ENSO) and Pacific Decadal Oscillation (PDO) teleconnections with

both the precipitation and spring discharge are analyzed and quantified.

To arrive at a deeper understanding about the dynamic behavior and storage mechanism in the karst system, besides recession coefficient estimates according to Maillet's equation, a single master recession curve is further generated by assembling the available time series of the Sarabkalan Spring discharge using the genetic algorithm approach presented by Gregor and Malík (2012).

Springshed and General Groundwater Flow Pattern

A combination of the water budget calculation, topography, and geological and tectonic settings was used to map the springshed of the Sarabkalan Spring. The springshed area was estimated to be \sim 87 km², according to Equation S2 in SI. The spring drains the groundwater from the Asmari Formation cropped out across SKA and SA. The springshed boundaries (Figure 1) were delineated based on (1) the estimated area for the springshed, (2) the topography map, and (3) the geological and tectonic settings. The springshed is bounded to the Gachsaran (to the northern and eastern portions) and Pabdeh (to the western portions and as bedrock) formations, and to the SA crest. Those portions of SKA and SA are considered as the springshed that are higher than the spring location (960 m) and also there is no barrier anywhere between them and the spring (Figure S4 in SI). Given the topography map and geometry of the Asmari Formation in both SKA and SA (Figure 1a), the springshed is classified into two subaquifers 1 and 2. Subaquiifer 1 constitutes the northern limb of SKA where it is separated from the rest of the springshed by the Pabdeh Formation at the core of SKA. Subaquiifer 2 contains the southern-limb of SKA and the northern-limb of SA as an integrated system.

Given the above evidence, the local groundwater initially flows along the dip of the bedding plain from the anticline axis toward the feet, and it tends to flow parallel to the anticline axis westward to eventually feed the Sarabkalan Spring (Figure 1a). As groundwater mostly moves parallel to the strike through the lower limbs (Figure 1a), it seems that two major conduit systems are separately developed on the SKA feet, where the branches of diffuse flow or small-conduit flow join each other (Ashjari and Raeisi 2006). The recession coefficients were calculated for seven selected recession curves from 2011 to 2019 (Table S1) to clarify the presence of the conduit system and identify the aquifer microregimes. The mean value of recession coefficients α_1 , α_2 , and α_3 are calculated to be 0.01539 (0.00782 to 0.03605), 0.00518 (0.00232 to 0.00838), and 0.00148 (0.00031 to 0.00529), respectively. Given three different recession coefficients indicates that in addition to diffuse flow through matrix and fractures, the conduit fast flow (corresponding to the large α_1) also contributes to the spring flowrate (Kresic and Stevanovic 2010). Figure S5 indicates that the steeper initial-recession coefficients are likely to be associated with those years of higher precipitations. This

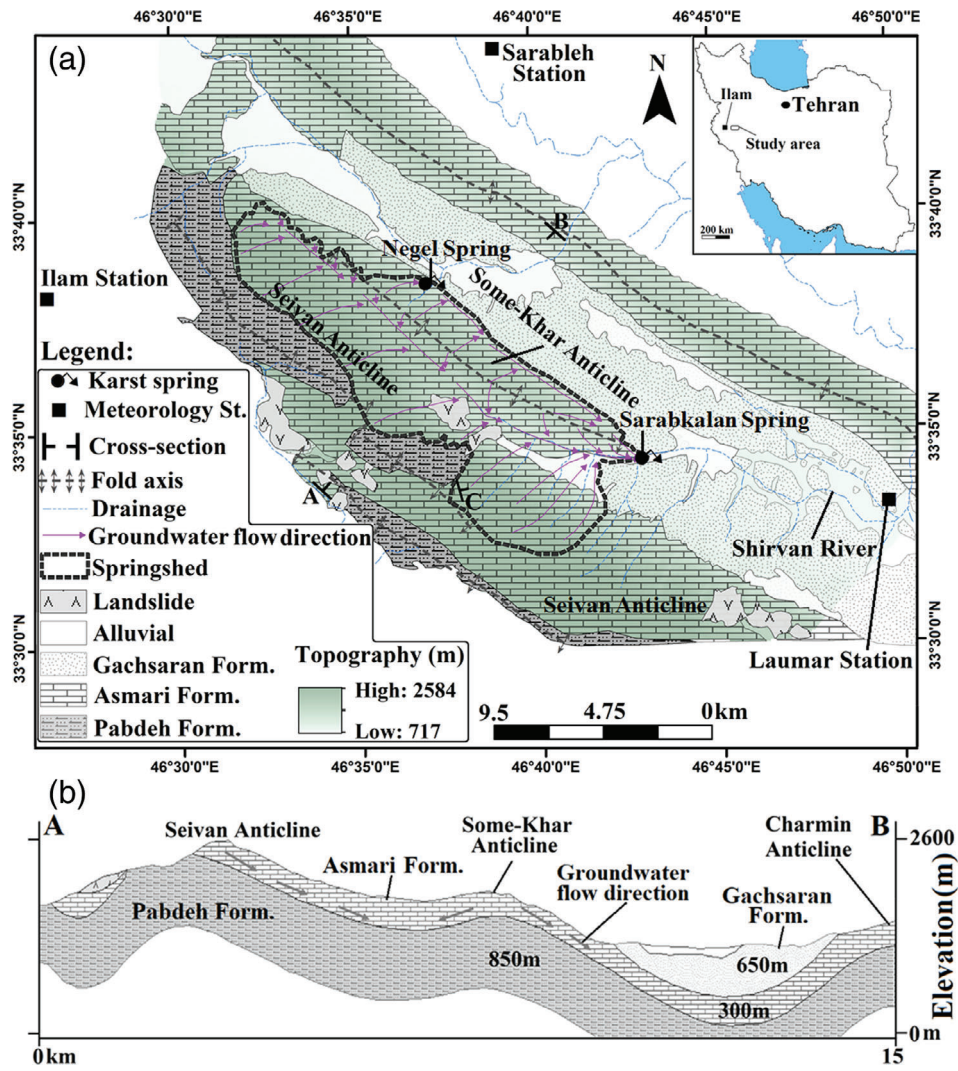


Figure 1. (a) Hydrogeology map of the area and (b) the simplified schematic geological cross-section.

probably results either from greater water table gradients or from the contribution of larger conduits/fractures to water transfer to the spring.

Overall, it was found that the springshed ($\sim 87 \text{ km}^2$) contains two subaquifers, each with its own general groundwater flow direction, parallel to the anticline's axis, which ends to the Sarabkalan Spring. It seems that karst conduit(s), contributing to the initial recession coefficient (α_1), is also developed in each subaquifer along the major flow direction at the lower limbs of SKA.

Precipitation, Discharge, and Recession Curve

Over the most recent 4 years, both the average precipitation across the springshed and the discharge of the Sarabkalan spring increased compared to the 2008–2014 period (Figure 2).

The largest lag-correlation coefficient between precipitation and spring discharge is statistically estimated to be 0.67, associated with ~ 99 d delay time (Figure S6). To calculate the lag-correlation, the standardized-departure series were used rather than the original series. The standardized-departure series were obtained

from a preprocessing procedure introduced by Hanson et al. (2004), as explained in the “methodology in further details” in SI. Looking carefully at Figure 2, it can be shown that the pulses from the initial precipitations (i.e., over the late autumn and early winter) would manifest in the spring with larger time lag than those from the late precipitations. The plausible explanations are that (1) in autumn and wintertime, precipitation at high-elevation portions of the springshed predominantly occurs as snow, so that, the recharge rate is not significant (Karimi et al. 2018), (2) the soil moisture of the unsaturated zone is at its minimum level (Figure S7 in SI); thus, the initial rain waters tend to be mostly stored in this zone (Karimi et al. 2003), and (3) in the early autumn, the water table is usually at its deepest state (i.e., the thickest unsaturated zone). As an example, in the 2018–2019 hydrological year with high-frequency rainfall events and denser discharge records, the time lag between the initial intense precipitation (October 10, 2018) and its corresponding spring response (January 29, 2019) is as much as 111 d, while the second-largest flow peak (April 14, 2019) occurred 13 d after the intense precipitation at April 1, 2019

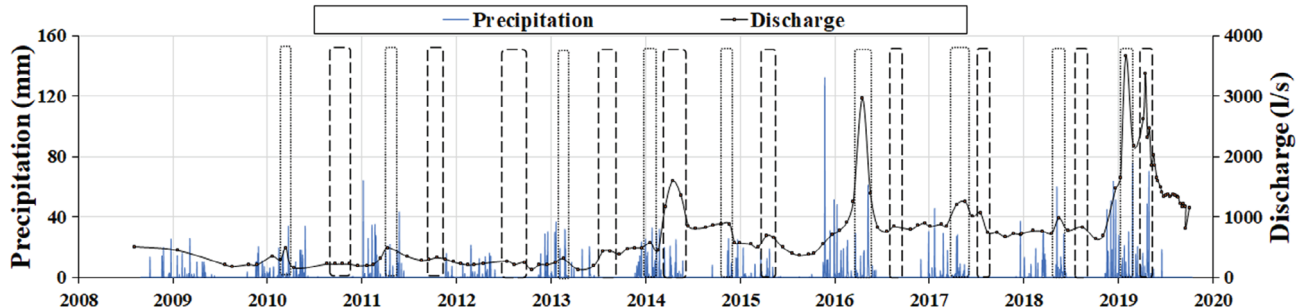


Figure 2. Precipitation versus the Sarabkalan Spring hydrograph from 2008 to 2019. The thin-dashed and thick-dashed boxes show the two main flow peaks for each hydrological year.

(~100 mm). In reality, the intense precipitations over the late winter and springtime could then quickly have flushed the water previously stored in the unsaturated zone toward the major fractures or probable hidden shafts. They could either transmit water vertically to the water table or push the water table toward the spring through conduit fast flow (Karimi et al. 2003; Giese et al. 2018). Table S1 clearly shows that the larger recession coefficients are associated with the hydrological years of greater discharge (i.e., higher water table), such as 2015–2016.

Figure 2 also shows that the spring has two main flow peaks over each hydrological year. The first one (thin-dashed boxes) usually occurs either in the late winter or early springtime while the second one (thick-dashed boxes) occurs over the dry season in smaller amplitude. These findings are also confirmed by the hydrochemistry and stable isotopes characteristics, as explained in the following sections. The second flow peak observed over the dry season is an interesting typical case for the Zagros Mountains that has not been reported in previous studies (Raeisi and Karami 1997; Karimi et al. 2003, 2005, 2018; Vardanjan et al. 2018).

The master recession curve from the genetic algorithm analysis on all the existing data from 2008 to 2019 further demonstrates that the karst groundwater system has two principal portions, discharging into the given spring with different time lags (Figure S8). The master recession curve has multiple portions (i.e., multiple breakpoints), reflecting changes in water flows characteristic of the karst aquifer (Bonacci 1993). In practice, one can depart the master recession curve into two principal segments, each with its own segments. The first principal segment has three different recession coefficients, consistent with conduit, fracture, and matrix storages, respectively. The second principal segment has two different recession coefficients. These findings are well-matched against the two principal flow peaks over each hydrological year (Figure 2). The plausible explanation is that the first peak can most probably be associated with the water draining from a broad portion of the springshed, relatively closer to the spring, which contains subaquifer 1 coupled with a broad portion of subaquifer 2. The second peak rather originates from the water coming from the far-distance portions of subaquifer 2 (i.e., the northwest end) which has a deepest water table (i.e., thickest unsaturated zone),

highest elevation, and most snowfall during autumn and winter. The lower electrical conductivity (EC), Ca + Mg, HCO₃, and δ¹⁸O observations in the spring water during the second flow peak may confirm the idea.

Water Chemistry

Generally, the temporal variations in pH and EC of the spring water are roughly reciprocal. In this regard, EC decreases with increasing pH during high flowrates (Figure 3) due to higher pH and lower EC of the fresh rain water. Figures 3 and S8 show that EC roughly has two main signals over each hydrological year (specifically in 2016–2017 and 2017–2018): the first signal from the early autumn to the late winter and the second from springtime to late summer (blue flashes in Figure S9). In each signal, EC begins uprising to reach its peak and then starts falling. Such behavior is roughly consistent with the two principal flow peaks, when the lowest EC of each hydrological year (blue-dotted circles in Figure S9) occurs over summer, corresponding to an increase in the discharge (as shown in Figure 2) but a delay in time. The highest EC values occurred in 2016–2017 of the smallest annual precipitation because of (1) higher residence time of water under lower recharge rates, (2) the greater participation of matrix flow to feed the spring, (3) the lower dilution effect of high-quality water produced by the Asmari Formation, and (4) the stronger degradation effect of the Gachsaran Formation covering SKA and SA flanks.

In Figures 3 and S8, the dashed boxes highlight the spring water response to some intense precipitation. In the spring, the discharge begins to increase while the EC, Ca + Mg, HCO₃, SO₄, Cl, and ionic strength tend to decline after intense precipitation owing to the dilutive nature of fresh rain water. This relatively quick response of the spring agrees well with the hypothesis of the conduit fast flow contribution to the spring flowrate.

Most parameters, particularly EC and sulfate concentration, show more variations over the wet season compared to the dry season (Figure 3). The higher variations in sulfate are in part due to the mixing between groundwater of different sources, such as the water from Asmari limestone and Gachsaran formations (Karimi et al. 2005). Leaching from the Gachsaran can increase the sulfate concentration and destroy water quality because it contains

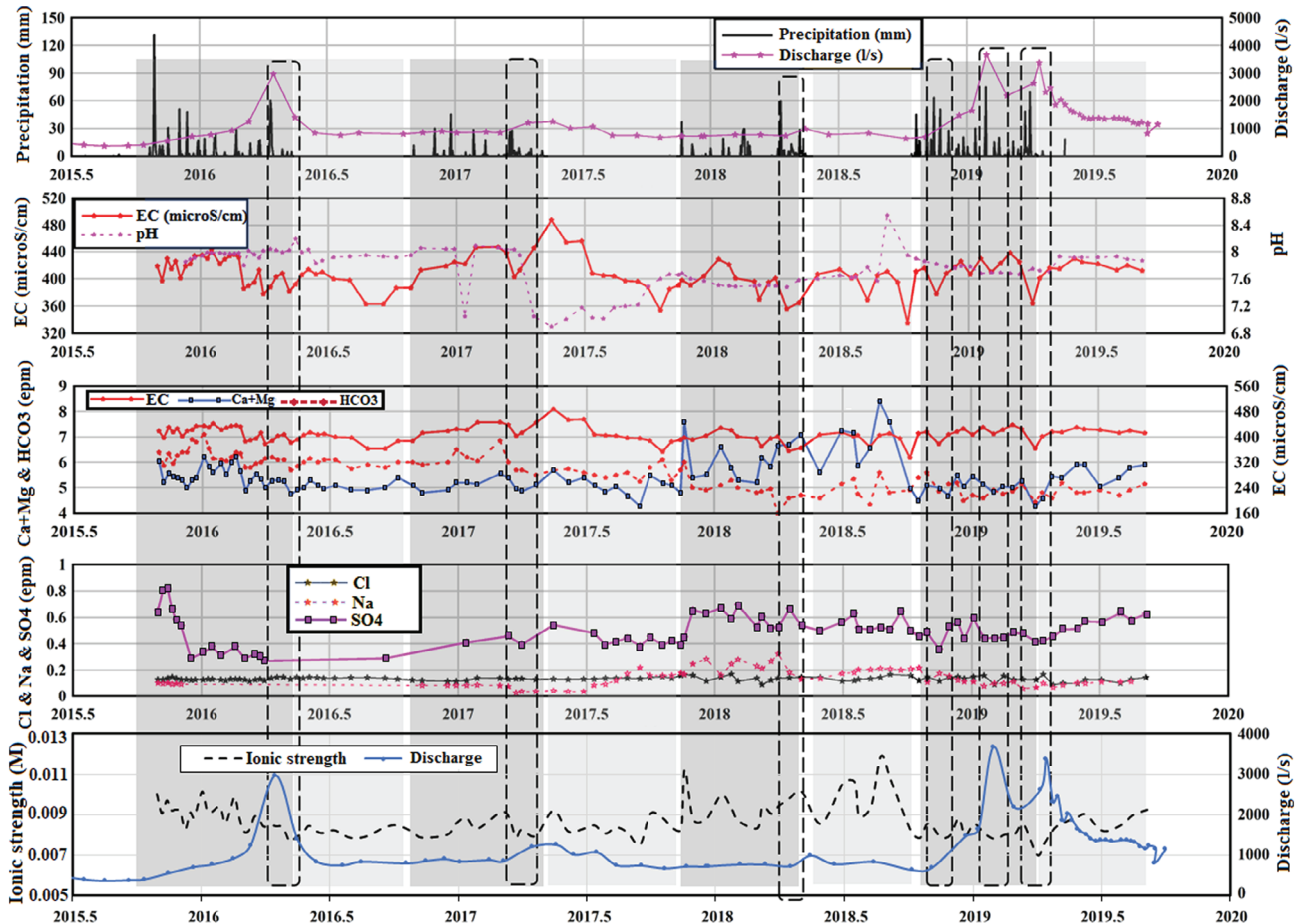


Figure 3. Hydrograph and chemographs for the Sarabkalan Spring water from 2015 to 2019.

evaporative rocks with high solubility (Karimi et al. 2005; Rezaei et al. 2017). There are some notable points regarding sulfate concentration. *First*, its concentration varies from year to year as 2015-2016 and 2017-2018 hydrological years have roughly the highest sulfate concentrations. *Second*, the temporal variations in the sulfate concentration are more substantial over wet seasons compared to dry seasons. The wet seasons of the dry years 2016-2017 and 2017-2018 are associated with an increase in the sulfate content while the sulfate content decreased over the wet season of the extremely wet year 2018-2019. *Third*, the sulfate concentration varies relatively after each intense precipitation. It may either increase or decrease after the most intense precipitations (>40 mm). The dotted boxes in Figure 3 show that the spring's sulfate increased after the intense precipitations of the early wet season of 2015-2016 and the late wet season of 2017-2018 while it decreased after all other intense precipitations. The increase in sulfate over early 2015-2016 is due to intense precipitation of ~ 132 mm (Figure 2) that occurred after the dry year of 2014-2015 (264 mm in Table S1). Also, the intense precipitation in the late wet season of 2017-2018 occurred after a dry ~ 45 d period (no precipitation) within the winter. In reality, the Gachsaran Formation is more dissolvable after either dry years or periods with no precipitation because it has lower water content and

poor vegetation coverage. Besides, it would experience stronger mechanical erosion by winds and anthropogenic activities. On the other hand, the dilutive role of high-quality water which comes from the Asmari Formation is lower during the initial precipitations. After a relatively long period with no precipitation, the unsaturated zone tends to be thicker and drier; it therefore takes a longer time to the fresh rain water to reach the spring and to dilute the degradation effect of the Gachsaran Formation.

Given the above evidence, it seems that the sulfate concentration in the spring water is controlled by the ratio of the water coming from the leaching of the Gachsaran Formation to that produced by the Asmari Formation. Generally, during wet seasons, runoff produced over the Gachsaran Formation can inversely affect the spring because it crops out in the flanks near the spring. The high-volume water produced by the Asmari limestone over the late wet season, particularly during wet hydrological years, can substantially dilute the sulfate concentration.

Figure S10 illustrates that the sum of calcium and magnesium (as main cations) and the sum of bicarbonate and sulfate (as main anions) are highly correlated because carbonate ($\text{Ca}-\text{Mg}-\text{HCO}_3$ type) and gypsum ($\text{CaSO}_4 \cdot 2\text{H}_2\text{O}$) are the main constituents of the Asmari and Gachsaran formations, respectively. EC further tracks variations in both the sum of calcium and magnesium

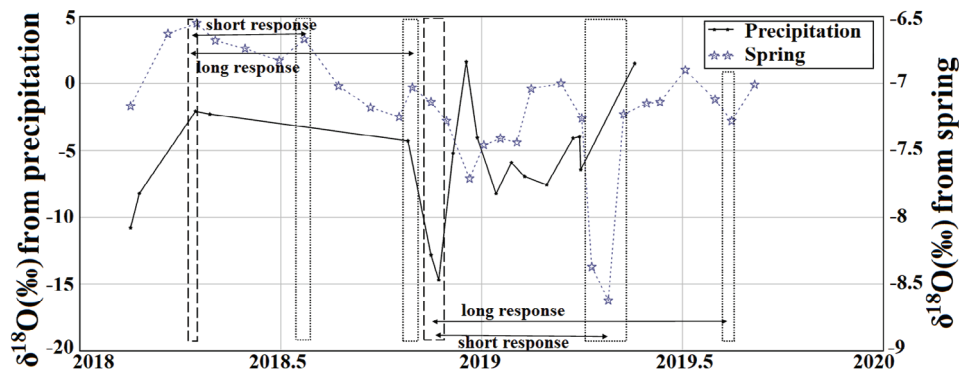


Figure 4. Comparison of the $\delta^{18}\text{O}$ graphs from rainfall with the Sarabkalan Spring's water. The thick-dashed boxes show the peaks in rainfall, and the thin-dashed boxes display their corresponding response in the spring water.

and the sum of carbonate and sulfate. The blue boxes highlight those periods during which EC, Ca + Mg, and SO₄ + HCO₃ are corresponding.

$\delta^2\text{H}$ and $\delta^{18}\text{O}$ Isotopes from Rainfall and Spring Water

Figure S11 shows that $\delta^2\text{H}$ and $\delta^{18}\text{O}$ measurements from rainfall and the Sarabkalan, Sero, and Negel spring's water overlap with the Mediterranean Meteoric Water Line, MMWL (Gat and Carmi 1970), confirming that the meteoric conditions in the area are mainly controlled by the Mediterranean weather condition. In Figure S11, isotopic data of the spring waters from the Sarabkalan, Sero, and Negel fall close to each other, along the local meteoric water line (LMWL). This suggests that *firstly* precipitation, as the only source for the spring, percolates through karst aquifer without experiencing significant evapotranspiration, and *secondly* the three springs roughly share the same springshed. That being said, the Sero Spring, emerging intermittently in the immediate vicinity of the Sarabkalan Spring (Figure S1 in the SI) over high volume-discharge periods of wet years, serves as an overflow of the Sarabkalan Spring.

Similar to the discharge, Figure 4 shows that $\delta^{18}\text{O}$ measurements from the Sarabkalan Spring, besides the main peak over the wet season (with a shorter time lag), have another peak in summer (with a longer time lag and smaller degree). To estimate the time lag between rainfall and the Sarabkalan Spring discharge, two sinusoidal models were fitted to the $\delta^{18}\text{O}$ series from both rainfall and the spring water based on Equation S3 in SI. Given that there was no precipitation over the dry season from May to late October 2018 and that the spring water' $\delta^{18}\text{O}$ data set does not show a typical seasonal behavior, the sinusoidal models were first fitted to the collected data from late October 2018 to September 2019 (Figure S12). Then, the lag-correlation coefficient of ~ 0.85 is estimated from the sinusoidal lines, which corresponds to the precipitation signal manifesting in the spring water after ~ 145 d (Figure S13). The second-largest correlation is also computed to be ~ 0.61 corresponds to the time lag of ~ 40 d. Furthermore, the time lag between the sharp signals of the rainfall and spring water' $\delta^{18}\text{O}$ (Figure 4) is calculated to be as much as ~ 154 d, which is close

to the 145 d obtained from the lag-correlation calculation. Notably, the high flow discharges are likely associated with a depletion in $\delta^{18}\text{O}$ (Figure S14 in SI), reflecting the large volume of the spring water over the high discharge period that comes from the higher elevations. In fact, the rainfall $\delta^{18}\text{O}$ composition (i.e., percolation) from higher elevations is lighter. The $\delta^{18}\text{O}$ signal manifested in the discharge over the springtime is sharper compared to that of summer (Figure 4), consistent with the principal flow peaks. As mentioned, a large volume of the conduit-flow type originates from the new rain water discharges to the spring over late winter or early springtime. Therefore, the sharper response of the spring over early springtime compared to the wintertime is reasonable. The $\delta^{18}\text{O}$ signal in the spring water during summer rather results from precipitation (mainly as snowfall during autumn and winter) falling at the high-elevation portions of subaquifer 2, corresponding to the second flow peak. The other notable point is that the amplitude of $\delta^{18}\text{O}$ variations in the Sarabkalan Spring is generally smaller compared to those of rainfall (Figure 4), because the isotopic composition signals from precipitation attenuate during infiltration through the soil, particularly in the vadose zone, and mixing with the restored karst water (Kresic and Stevanovic 2010).

ENSO and PDO Controls on Precipitation and Spring Discharge

Here, the relationship between the ENSO and PDO climate indices and both the long-term (1986-2019 at Ilam Station) and short-term (2008-2019 at Laumar Station, the closest station to the Sarabkalan Spring) precipitation and karst spring discharge is explored. The CWT on long-term precipitation of the area (e.g., Ilam station) shows two principal periodicities: annual- and > 8 -year-period (Figure S15). In addition to a 6-month-period signal from 2013-2019, the Sarabkalan Spring discharge shows a signal of a 1.5-year-period from 2014 to 2017 at the CWT. Furthermore, the WTC results demonstrate that the annual and > 8 -year-period signals of precipitation are largely controlled by PDO, while ENSO influences the 2-6- and > 8 -year signals. Precipitation has strong coherence (at the 5% significant level) with ENSO in the WTC

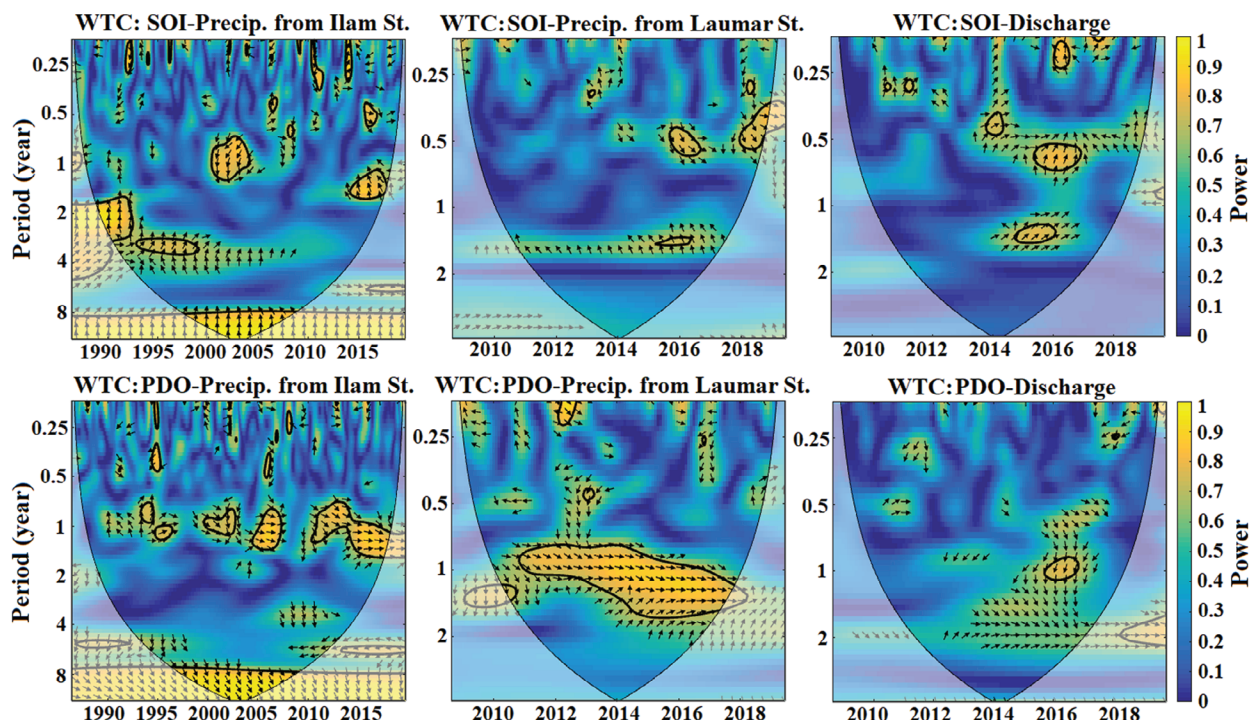


Figure 5. WTC between ENSO and PDO climate indices and precipitation in both the Ilam and Laumar stations. The oldest indicator of ENSO state is the Southern Oscillation Index (SOI). The color bars indicate the coherence. The thick black curves reveal the 5% significance level, and the less intense colors denote the cone of influence (COI). Black arrows show the phase angle, characterizing the in-phase (right-pointing arrows) and antiphase (left-pointing arrows) relations. Up- or down-pointing arrows are also indicative of lead-lag between the time series (Grinsted et al. 2004).

at the >8-year band, spanning the whole study period 1986–2019 (Figure 5). From the long-term precipitation analysis, it is clear that a moderate to strong coherence (0.5 to 1) exists between precipitation and ENSO at the 2–6-year band. From the short precipitation of the latest years (2008 to 2019), the seasonal to annual precipitation has moderate to strong coherence with ENSO at the 0.25 to 1-year bands from 2013 to 2019. Furthermore, precipitation has moderate to strong coherence with ENSO at the 1- to 2-year bands from 2008 to 2018. The teleconnection between PDO and precipitation is more specific compared to the ENSO. Two principal bands for which precipitation has a strong coherence with PDO are observable: the annual and the >8-year. The long-term precipitation at the Ilam Station has strong coherence with PDO at the 1- and >8-year bands over the whole period from 1986 to 2019. The short-term precipitation analysis at the Laumar Station also highlights the strong coherence between PDO and precipitation in the WTC at 0.7- to 2-year bands from 2008 to 2019. Comparing ENSO and PDO climate indices with historical precipitation in the area (Figure S15) signifies that when the positive peaks in PDO are coupled with El Niño, severe precipitations occur in the area. As an example, the highest annual precipitation at the Laumar Station occurred in 2018–2019 (848 mm), 2015–2016 (836 mm), 2013–2014 (503 mm), and 2009–2010 (458 mm) that roughly correspond to positive (or near positive) PDO and negative Southern Oscillation Index (SOI) (i.e., El Niño phase of ENSO).

Interestingly, both precipitation and spring discharge significantly increased after mid-2014, consistent with the coupled positive PDO and negative SOI. Note that the negative SOI (i.e., El Niño phenomena) is almost associated with an increase in precipitation over western Iran (Alizadeh-Choobari and Najafi 2018).

Accordingly, the WTC analysis also shows that the spring discharge is relatively controlled by both ENSO and PDO climate indices (Figure 5). The seasonal periodicities in the spring discharge are largely controlled by ENSO, while the annual periodicities (1- to 2-year) are rather highly related to PDO. The spring discharge has moderate to strong coherence with ENSO at ~0.25- to 0.8-year bands from 2013 to 2019. Furthermore, moderate to strong (0.5 to 1) coherence exists between the spring discharge and PDO in the WTC at the ~2-year period over the whole study period (2008 to 2019). Moreover, there exists strong coherence at a 5% confidence level between the discharge and PDO in the WTC at a ~1-year band from 2015 to 2017. Figure S16 clearly shows that the main flow peaks in the historical discharge at the Sarabkalan Spring are associated with positive peaks in PDO and negative phases of SOI, consistent with the results of the precipitation wavelet analysis. The WTC analysis further shows that precipitation and the spring discharge have moderate to strong coherence with each other at seasonal- to 3-year period band over all the study period, whereas strong coherence at 5% confidence level occurred from 2012 to 2019.

Conclusions

This study demonstrates that the Sarabkalan spring-shed is a coupled diffuse-conduit karst system where conduits developed along the lower limbs of the anticlines of SKA and SA; based on (1) the existence of at least two long groundwater flow lines parallel to SKA and SA; (2) the high discharge of spring, particularly in the wet hydrological years, indicating the presence of such conduits for conveying a large volume of water (up to 3866 L/s); (3) the presence of three different recession coefficients in which the steepest is more probably consistent with the karstic conduits; and (4) the relatively quick decrease in EC, Ca + Ma, SO₄, and Cl after intense precipitations which can most probably be attributed to the karstic conduits.

The Sarabkalan Spring exhibits its own specific behavior, which is different from the karst systems previously studied in Zagros. Its springshed consists of two subaquifers 1 and 2. The spring hydrograph shows two principal peaks over almost hydrological years. The close-distance portions of the springshed, containing entire subaquifer 1 and a broad portion of subaquifer 2, are discharged to the spring over the late winter and early springtime to create the first peak. In contrast, water from the far-distance portions of subaquifer 2 reaches the spring over the summertime, creating the second-peak with a lower sharpness.

It is further discovered that precipitation and, in turn, the spring discharge have long-term (>8-year) oscillations beyond the short-term (e.g., annual) periodicities. Both the short- and long-term periodicities significantly correlate with PDO and ENSO. The precipitation coherency with PDO is more evident than that with ENSO. Notably, it is observed that over the positive phase of PDO coupled with El Niño phenomena, both precipitation and spring discharge tend to increase, signifying the significant influence of the atmospheric circulations of the Pacific Ocean on the hydroclimate events in the springshed.

This study demonstrates that the behavior of each karst system, beyond the hydrogeological, morphological, hydrochemical factors, which are specified in each system, are controlled by the large-scale climate variability, which may occur 1000 km far away from the area of interest. This paper highlights the necessity of a combination of hydrogeological and climatic-oceanic-atmospheric factors from the local to global scales for optimal management of karst water resources.

Acknowledgments

I am grateful to Ilam Regional Water Authority for providing the hydrologic and hydrogeological data used in this study. The author would also like to thank Mrs. Fahimeh Haji and Mr. Hasan Rezaei for their help in collecting samples. My appreciation goes to Costantino Masciopinto and two anonymous reviewers for their insightful comments, which greatly improved this manuscript.

Author's Note

The author(s) does not have any conflicts of interest.

Supporting Information

Additional supporting information may be found online in the Supporting Information section at the end of the article. Supporting Information is generally *not* peer reviewed.

Figure S1. The locations of both the Sarabkalan Spring and Sero Spring in the Sarabkalan Village where the springs are 60 m apart. The two production wells are also shown.

Figure S2. The proposed conceptual model based on geometry and output location in the Zagros Mountains by Ashjari and Raeisi (2006). Group N: No hydraulic connectivity between the two limbs. Group C: Hydraulic connectivity between two limbs. The subgroups P, L, R, and N show the outflow positions, Down-plunge Nose, Limbs, Rivers, and Combination respectively.

Figure S3. The long-term daily precipitation records from the Ilam Station as it has the longest measurements in the area. It is to be noted the highest annual precipitation (1056 mm) fallen in the hydrological year 2018-2019 which is about twice the long-term annual average rainfall.

Figure S4. The cross-section between the Seivan Anticline (point C) and the Sarabkalan Spring in Figure 1, which demonstrates no barrier between these two points.

Figure S5. Annual precipitation versus the initial recession coefficients obtained from the selected typical-hydrographs of the Sarabkalan Spring for different the hydrological years. The values are also listed in Table S1.

Figure S6. (a) The lag-correlation between the standardized-departure series of precipitation (from the Laumar Station) and discharge of the Sarabkalan Spring for a period from 1 August 2008 to 1 October 2019. (b) The comparison of the standardized-departure series from both precipitation and shifted-precipitation with the standardized-departure from the spring discharge.

Figure S7. The mean monthly soil moisture time series for the area obtained from ESA CCI archives.

Figure S8. The master recession curve obtained from the genetic algorithm analysis on hydrograph of the Sarabkalan Spring from 2008 to 2019.

Figure S9. EC versus precipitation. Blue flashes show the general trend of EC and blue circles highlight low conductivity EC events that notably occurred over the dry season.

Figure S10. EC variations versus the chemographs from both the sum calcium and magnesium and the sum of sulfate and bicarbonate.

Figure S11. $\delta^{18}\text{O}\%$ vs. $\delta^2\text{H}\%$ measurements from precipitation and the Sarabkalan, Sero, and Negel spring's water. LMWL is the best fit for precipitation samples: $\delta^{18}\text{O}\% = 7.665 \delta^2\text{H}\% + 23.855$. The Mediterranean meteoric water line (MMWL): $\delta^{18}\text{O}\% = 8 \delta^2\text{H}\% + 22$.

Figure S12. The sinusoidal models fitted to the weighted $\delta^{18}\text{O}$ from precipitation (a) and $\delta^{18}\text{O}$ from the Sarabkalan Spring's water (b) over the period from October 2018 to September 2019.

Figure S13. The lag-correlation between the sinusoidal models fitted to the $\delta^{18}\text{O}$ from both precipitation and the spring discharge. The largest correlation is ~ 0.85 that occurred at a lag time of 145 days. The second-largest correlation is obtained to be ~ 0.61 , corresponding with the lag time of 40 days.

Figure S14. $\delta^{18}\text{O}$ from the Sarabkalan, Sero, and Negel spring versus (a) precipitation, and (b) the Sarabkalan Spring hydrograph.

Figure S15. Continuous wavelet transform (CWT) for precipitation from both the Ilam (long-term) and Laumar (short-term) stations and for the Sarabkalan Spring discharge.

Figure S16. The comparison of the ENSO and PDO climate indices with historical records from precipitation (a) and the spring discharge (b) in the area.

Figure S17. Four preprocessing steps of (a) regular interpolating the data via using a spline, (b) transforming the interpolated records to cumulative departures series, (c) capturing the residuals of the cumulative departure series by subtracting a regression-fitted low-order polynomial, and finally (d) normalizing the residuals by the historic mean for the spring discharge data.

Table S1. Recession coefficients α_1 , α_2 , and α_3 calculated from 7 typical recession curves (one per year) from 2010 to 2019, according to Maillet's equation. The spring discharge values refer to Q_0 in Equation S1 for α_1 . Mean annual recharges are related to all the hydrological year.

References

- Alizadeh-Choobari, O., and M.S. Najafi. 2018. Climate variability in Iran in response to the diversity of the El Niño–Southern Oscillation. *International Journal of Climatology* 38, no. 11: 4239–4250.
- Ashjari, J., and E. Raeisi. 2006. Influences of anticlinal structure on regional flow, Zagros, Iran. *Journal of Cave and Karst Studies* 68, no. 3: 118–129.
- Bonacci, O. 1993. Karst springs hydrographs as indicators of karst aquifers. *Hydrological Sciences Journal* 38, no. 1: 51–62.
- Diodato, N., L. Guerriero, F. Fiorillo, L. Esposito, P. Revellino, G. Grelle, and F.M. Guadagno. 2014. Predicting monthly spring discharges using a simple statistical model. *Water Resources Management* 28, no. 4: 969–978.
- Ford, D., and P. Williams. 2007. *Karst Hydrogeology and Geomorphology*. Chichester, UK: John Wiley & Sons Ltd.
- Gat, J.R., and I. Carmi. 1970. Evolution of the isotopic composition of atmospheric waters in the Mediterranean Sea area. *Journal of Geophysical Research* 75, no. 15: 3039–3048.
- Giese, M., T. Reimann, V. Bailly-Comte, J.C. Maréchal, M. Sauter, and T. Geyer. 2018. Turbulent and laminar flow in karst conduits under unsteady flow conditions: Interpretation of pumping tests by discrete conduit-continuum modeling. *Water Resources Research* 54, no. 3: 1918–1933.
- Green, T.R., M. Taniguchi, H. Kooi, J.J. Gurdak, D.M. Allen, K.M. Hiscock, H. Treidelg, and A. Aurelig. 2011. Beneath the surface of global change: Impacts of climate change on groundwater. *Journal of Hydrology* 405, no. 3–4: 532–560.
- Gregor, M., and P. Malík. 2012. Construction of master recession curve using genetic algorithms. *Journal of Hydrology and Hydromechanics* 60, no. 1: 3–15.
- Grinsted, A., J.C. Moore, and S. Jevrejeva. 2004. Application of the cross wavelet transform and wavelet coherence to geophysical time series. *Nonlinear Processes in Geophysics* 11, no. 5–6: 561–566.
- Hanson, R.T., M.W. Newhouse, and M.D. Dettinger. 2004. A methodology to assess relations between climatic variability and variations in hydrologic time series in the southwestern United States. *Journal of Hydrology* 287, no. 1–4: 252–269.
- Huo, X., Z. Liu, Q. Duan, P. Hao, Y. Zhang, Y. Hao, and H. Zhan. 2016. Linkages between large-scale climate patterns and karst spring discharge in Northern China. *Journal of Hydrometeorology* 17, no. 2: 713–724.
- Karimi, H., E. Raeisi, and A. Rezaei. 2018. Determination of karst aquifer characteristics using physicochemical parameters (A case study from west of Iran). *Geopersia* 8, no. 2: 293–305.
- Karimi, H., E. Raeisi, and M. Bakalowicz. 2005. Characterising the main karst aquifers of the Alvand basin, northwest of Zagros, Iran, by a hydrogeochemical approach. *Hydrogeology Journal* 13, no. 5–6: 787–799.
- Karimi, H., E. Raeisi, and M. Zare. 2003. Hydrodynamic behavior of the Gilan karst spring, west of the Zagros, Iran. *Cave and Karst Science* 30, no. 1: 15–22.
- Kresic, N., and Z. Stevanovic. 2010. *Groundwater Hydrology of Springs: Engineering, Theory, Management and Sustainability*, Vol. 565. Amsterdam, the Netherlands: Elsevier.
- Lakey, B., and N.C. Krothe. 1996. Stable isotopic variation of storm discharge from a perennial karst spring, Indiana. *Water Resources Research* 32, no. 3: 721–731.
- Raeisi, E., and G. Karami. 1997. Hydrochemographs of Berghan karst spring as indicators of aquifer characteristics. *Journal of Cave and Karst Studies* 59, no. 3: 112–118.
- Rezaei, A., and J.J. Gurdak. 2020. Large-scale climate variability controls on climate, vegetation coverage, Lake and groundwater storage in the Lake Urmia watershed using SSA and wavelet analysis. *Science of the Total Environment* 724: 138273.
- Rezaei, A., H. Karimi, and H. Zhan. 2017. The importance of understanding the hydrogeology and geochemistry of karst terrains for safely siting dams. *Journal of Cave and Karst Studies* 79, no. 1: 48–58.
- Rezaei, A., M. Zare, E. Raeisi, and R.N. Ghanbari. 2013. Interaction of a fresh water lake and a karstic spring via a syncline fold. *Groundwater* 51, no. 2: 305–312.
- Rusjan, S., K. Sapač, M. Petrič, S. Lojen, and N. Bezak. 2019. Identifying the hydrological behavior of a complex karst system using stable isotopes. *Journal of Hydrology* 577: 123956.
- Toran, L., and C.E. Reisch. 2013. Using stormwater hysteresis to characterize karst spring discharge. *Groundwater* 51, no. 4: 575–587.
- Vardanjani, H.K., M. Chitsazan, D. Ford, H. Karimi, and A. Charchi. 2018. Initial assessment of recharge areas for large karst springs: A case study from the central Zagros Mountains, Iran. *Hydrogeology Journal* 26, no. 1: 57–70.